Far-infrared laser study of magnetic polaritons in FeF_2 and Mn impurity mode in FeF_2:Mn

R. W. Sanders,* R. M. Belanger, M. Motokawa,† and V. Jaccarino
Department of Physics, University of California, Santa Barbara, California 93106

S. M. Rezende
Department of Physics, University of California, Santa Barbara, California 93106
and Departmento de Fisica, Universidade Federal de Pernambuco, Recife, Brazil 50.000

(Received 30 July 1980)

From a high-resolution, far-infrared laser study of the antiferromagnetic resonance (AFMR) of FeF_2, it is shown that a *magnetic polariton* model not only reproduces the broad (~4 kOe) complex structures observed in transmission, but is essential to the determination of the intrinsic (radiative and nonradiative) contributions to the linewidth. For the purest FeF_2 crystal an upper bound of 20 Oe for ΔH was found. The polariton model is extended to include the effects of Mn impurities. The theory correctly predicts the observed frequency pulling of host and impurity modes as a function of Mn concentration c and the large enhancement of the impurity-mode signal. From their dependence on c and sample thickness t the super-radiance and impurity-impurity contributions to ΔH_{imp} are separately obtained and compared with recently developed theories. The thermal relaxation of the host AFMR is shown to arise from four-magnon scattering.

I. INTRODUCTION

Only in recent times has an understanding evolved of the fundamental processes that contribute to the relaxation of the uniform-mode antiferromagnetic resonance (AFMR) and other long-wavelength modes in an antiferromagnetic (AF). In fact, quantitative comparison between experiment and theory in this regard has been confined largely to MnF_2, in which AFMR linewidth[1-3] and parallel pumping[4] studies were made in the microwave (9–24 GHz) region. For example, linewidths $0.05 \leq \Delta H \leq 20$ Oe, at $T \ll T_N$ have been obtained for the uniform and magnetostatic modes in highly polished disks of MnF_2 and have been shown to be associated with two-magnon scattering and radiation damping.[2] When one turns to the large anisotropy antiferromagnets which, because of the large gap at $k = 0$, necessarily must be studied in the far infrared (FIR)—examples are FeF_2 (Ref. 5) and CoF_2 (Ref. 6)—then broad asymmetric line profiles to the AFMR are found, sometimes extending over several kOe. [See data in Fig. 1(a).]

We have made a high-resolution study of the AFMR of FeF_2 using a FIR laser.[7] The transmission spectrum is shown to be describable in terms of the excitation of *magnetic polaritons,* the propagating coupled photon-magnon modes. The polariton description is found to be essential to understanding the intrinsic linewidth contributions. In addition, when Mn impurities are introduced substitutionally for Fe, a relatively broad and intense impurity mode appears, even at concentrations as low as 10^{-3} at.%. Because of the close proximity of the Mn impurity mode (1.509 THz) to the FeF_2 AFMR (1.575 THz), strong coupling between the two modes results. Using a coupled-equations-of-motion model, many details of the FeF_2:Mn system, including the origins of AFMR linewidth as well as interaction effects (such as

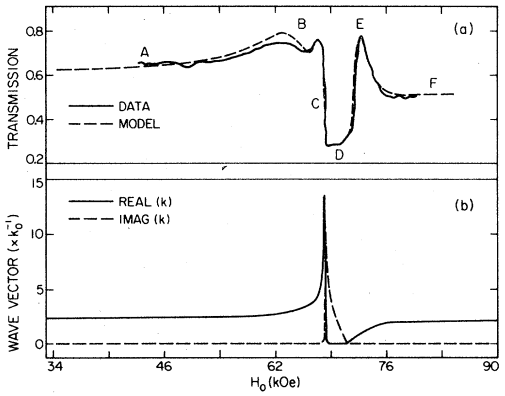

FIG. 1. Transmission of 1.36-THz radiation vs magnetic field H_0 is shown as the solid line in (a) for a 77 ± 2-μm thick sample of FeF_2 containing (0.0014 ± 0.0007) at.% Mn. Note the broad asymmetric line profile of the AFMR. The dashed line is the prediction of the polariton model (neglecting impurities) for $t = 77$ μm, $\epsilon = 5.4$, and $\Delta H = 20$ Oe. Spectral features $A-F$ are discussed in the text. In (b), the magnitude of the normalized wave vector k/k_0 of the propagating excitation vs magnetic field H_0 at 1.36 THz is plotted, using parameters appropriate for FeF_2. By comparison with the spectrum in (a) the important features of the data can be understood.

frequency-pulling and impurity-mode enhancement) between the two modes, may be quantitatively understood.

In Sec. II we describe the experimental arrangement, since the technique differs from the usual resonance methods and because the details of sample geometry, etc., influence the interpretation of the observed data. In Sec. III the magnetic polariton model is developed for the pure FeF_2 system, and it is compared to data for the host AFMR. Section IV introduces a coupled-equations-of-motion model which includes the effects of Mn impurities and compares its predictions to the experimental results. Section V consists of a discussion of the AFMR and Mn-impurity linewidths. A summary of our findings appears in Sec. VI.

II. APPARATUS

FeF_2 is a high-anisotropy, uniaxial AF; its AFMR in zero external field H_0 at $T=4.2$ K occurs at 1.58 THz, well in the FIR. (See Table I for parameters appropriate for FeF_2.) Since an external field H_0 of nearly 0.5 MOe would be required to shift the lower-branch AFMR to microwave frequencies, and no monochromatic FIR sources were available in this spectral region, earlier work has relied on Fourier-transform[6] or grating-spectrometer[5] techniques. With the advent of molecular gas lasers in the FIR, much higher resolution (<2 Oe) may be achieved by fixing the frequency at one of the available laser lines and sweeping the field generated by a superconducting solenoid.

The source in the current experiments is a cw, electron-pumped laser with cavity length 7.2 m and Michelson-type output coupling. In most of the experiments the lasing species is H_2O at 1.36 THz. However, some measurements were made using D_2O at 1.75 THz and DCN at 1.47, 1.54, and 1.58 THz. The location of these lines in relation to the resonance condition for the host and impurity modes is shown in Fig. 2. Because the power output is very sensitive to changes in mirror separation caused by thermal expansion and to changes in the pressure of the lasing medium, the cavity length of lasers of this type must be "tuned" to achieve stable lasing action. A portion of the laser output is monitored by a triglycine sulfate (TGS) pyroelectric detector. A phase-sensitive detection circuit and comparator are used to control a stepper motor which moves one mirror. This correction system maintains output power within 2% of a preset level for periods of several hours and has a short term (20 min) stability better than 0.5%. Light exiting the laser is mechanically chopped at 35 Hz and focused by a polyethylene lens into a light pipe of dry-nitrogen-flushed copper tubing. After passing through a polyethylene window, the light enters the magnet Dewar via a stainless-steel tube. Because of multiple scattering in the light pipe, the initially polarized light becomes totally unpolarized by the time it reaches the sample.

Details of the sample holder-detector are shown in Fig. 3. Samples are supported on a copper iris, which is thermally anchored to a copper block. Light passing through a sample is collected in a conical pipe and detected by a Ga-doped Ge bolometer placed outside the region of maximum field intensity. The field H_0, applied parallel to the direction of light propagation, is precisely measured and monitored by observing ^{27}Al NMR in a probe placed near the sample.

TABLE I. Values of relevant physical quantities in MnF_2 and FeF_2 are given (Ref. 9).

	MnF_2	FeF_2
H_E	528 Oe	555 Oe
H_A	8.37 kOe	191 kOe
M_S	576 Oe	560 Oe
H_C	92.9 kOe	501 kOe
a	4.87 Å	4.70 Å
c	3.30 Å	3.31 Å

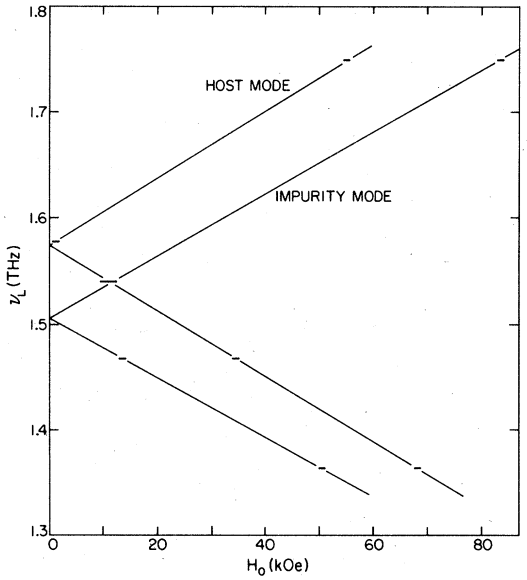

FIG. 2. Observed resonance fields are plotted vs laser frequency for both the host AFMR and Mn impurity mode in FeF_2:Mn with $c \simeq 0.01$ at.%. The lines are the least-squares linear fit to the data, from which the $c \simeq 0.01$ at.% data in Table II are determined.

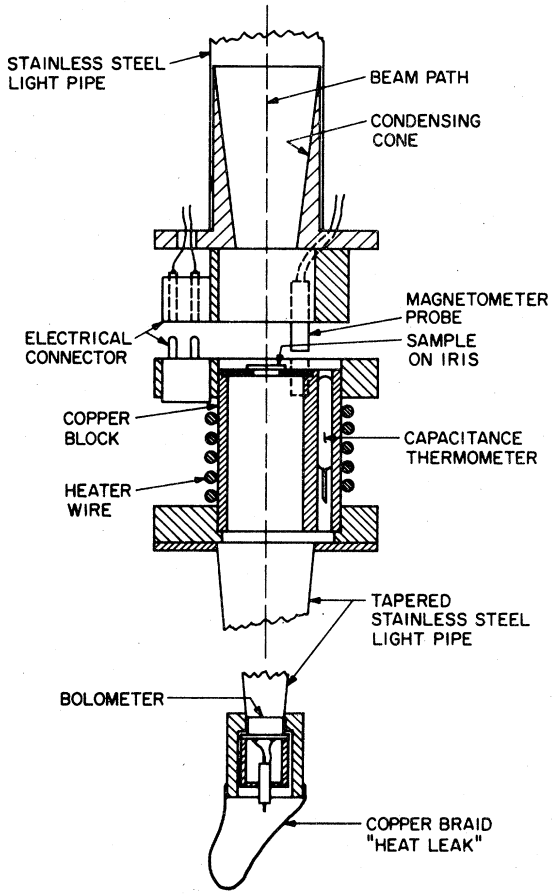

FIG. 3. Shown are details of the sample holder described in Sec. II. The assembly is placed in magnetic field H_0 directed parallel to the "beam path."

The samples are disk-shaped, single crystals typically 4 mm in diameter and 15 to 800 μm in thickness, with polished (<1 μm) faces normal to the C axis. The samples range in Mn concentration from $c \simeq 10^{-3}$ at.% to 8×10^{-1} at.%, as determined from the relative intensities of the impurity associated and host ^{19}F NMR spectra.[8]

For experiments at 4.2 K, helium gas surrounding the sample holder provides heat exchange with the liquid-helium bath. Sample temperatures up to 40 K are achieved by reducing the helium gas pressure and supplying current to a Constantan resistance heater, which is controlled by an ac capacitance bridge and a calibrated capacitance thermometer. The bolometer is maintained at 4.2 K by a copper braid "leak" to the liquid-helium-cooled walls of the sample tube. Additional details of construction and operation appear elsewhere.[9]

III. MAGNETIC POLARITONS

The AFMR of FeF_2 is in the FIR, where the radiation wavelength necessary to excite spin waves ($\lambda \simeq 0.1$ mm in FeF_2) is comparable to the thickness of typical samples studied. Therefore, it is inappropriate to use a point-sample approximation (as is customary in microwave experiments); rather, propagation of radiation through the sample must be considered. As an electromagnetic wave propagates, its associated electric ($\vec{E}$) and magnetic ($\vec{H}$) fields can excite internal degrees of freedom of the material. A *polariton* is the composite excitation which has its energy partitioned between the driving $\vec{E}$ or $\vec{H}$ field and the elementary excitations of the medium. In ordered magnetic systems, the $\vec{H}$ component of the radiation field couples to the long-wavelength spin waves (magnons). Therefore, *magnetic polaritons* are propagating coupled photon-magnon modes. Mills and Burstein[10] have reviewed the subject of polaritons involving elementary excitations of diverse origin. The derivation of the magnetic polariton dispersion will follow their treatment.

In an effective-field, equation-of-motion model, the frequency-dependent transverse susceptibility $\chi^{\pm} \equiv \chi_x \pm i\chi_y$ of a uniaxial ($C \parallel \hat{z}$) AF with $\vec{H}_0 \parallel C$ and rotating driving field $H_1^{\pm}$ is given by[11]

$$\chi^{\pm}(\omega) = 2H_A M_S / \{ H_C^2 - [(\omega/\gamma) \mp H_0]^2 \} \ , \qquad (1)$$

where ω is the angular frequency of the exciting electromagnetic field, $H_1^{\pm}$, γ is the gyromagnetic ratio, H_A is the sublattice magnetization, and H_C is the zero-field resonance frequency expressed in field units. When propagation of radiation through samples is considered, $\chi^{\pm}(\omega)$ enters the relevant Maxwell's equations

$$\vec{\nabla} \times \vec{H} = \frac{1}{c_0}\frac{\partial \vec{D}}{\partial t}, \quad \vec{\nabla} \times \vec{E} + \frac{1}{c_0}\frac{\partial \vec{B}}{\partial t} = 0 \qquad (2)$$

through the magnetic permeability tensor $\vec{\vec{\mu}}$ and leads to a dispersion for magnetic polaritons. Assuming plane-wave-like solutions, $\exp(i\vec{k}\cdot\vec{z} - i\omega t)$, with ω the frequency of the wave, $\vec{k}$ its wave vector, $\vec{z}$ the propagation direction, and c_0 the speed of light in a vacuum, Eqs. (2) become

$$\vec{k} \times \vec{H} = \frac{-\omega}{c_0}\vec{D}, \quad \vec{k} \times \vec{E} = \frac{\omega}{c_0}\vec{B} \ . \qquad (3)$$

In the linear-response regime

$$\vec{D} = \epsilon \vec{E}, \quad \vec{B}_\alpha = \sum_\beta \mu_{\alpha\beta}\vec{H}_\beta \ , \qquad (4)$$

with ϵ, the dielectric constant, taken to be real and isotropic. From Eqs. (3) and (4) the following rela-

tionship between $\vec{k}$ and ω is obtained:

$$\vec{k}\times(\vec{k}\times\vec{H})=-(\epsilon\omega^2/c_0^2)\vec{\vec{\mu}}\cdot\vec{H}\ . \tag{5}$$

Equation (5) becomes particularly simple if we choose rotating coordinates since in this representation $\vec{\vec{\mu}}$ is diagonal[10]:

$$\mu_{xx}=1+4\pi\chi^+;\ \ \mu_{yy}=1+4\pi\chi^-\ ;$$
$$\mu_{zz}=1;\ \ \mu_{ij}=0\ \text{ for } i\neq j\ . \tag{6}$$

Combining Eqs. (1), (5), and (6) we obtain the dispersion relation for magnetic polaritons

$$k^{\pm}=\frac{\omega}{c_0}\sqrt{\epsilon}\left[1+\frac{8\pi M_S H_A}{H_C^2-[(\omega/\gamma)\mp H_0]^2}\right]^{1/2}\ . \tag{7}$$

The poles $\omega_H^{\pm}$ of $\chi^{\pm}$ are the upper- and lower-branch resonant frequencies ($\omega_H^{\pm}/\gamma=H_C\pm H_0$). As shown in Fig. 4(a), important qualitative features of the polariton dispersion curve follow from Eq. (7). When ω is close to the AFMR frequency (ω_H), the propagating wave is a coupled mode of the electromagnetic field and the spin waves. Near $\omega_H^{+}(\omega_H^{-})$ a "forbidden band" exists of width $\Delta_{FB}=4\pi M_S H_A/H_C \simeq 2.8$ kOe in FeF_2, within which $k^+(k^-)$ has no real solutions. This region of strong coupling is particularly interesting, since information about the magnetic properties can be inferred by observing the transmitted radiation. However, in order to extract this information, it is necessary to examine the transmission problem in detail. In the region far-off resonance ($|\omega-\omega_H| >> \gamma\Delta_{FB}$) the dispersion approaches $k=\omega\epsilon^{1/2}/c_0$, the photon dispersion relation.

The complex wave vectors obtained in Eq. (7) are used to determine the transmission T through a plane parallel slab of thickness t (see Appendix A). It is convenient to express the result in terms of the real and imaginary part (η and κ, respectively) of the complex wave vector $\vec{n}=\vec{k}/k_0$, where $k_0\equiv\omega/c_0$. Using Eq. (A3) we may express T in the form

$$T=[16\epsilon^2(\eta^2+\kappa^2)\exp(-2k_0\kappa t)]/D\ , \tag{8}$$

where

$$D=\{[(\epsilon+\eta)^2+\kappa^2]^2+[(\epsilon-\eta)^2+\kappa^2]^2\exp(-4k_0\kappa t)$$
$$-2\exp(-2k_0\kappa t)[(\epsilon^2-\eta^2-\kappa^2)^2-4\epsilon^2\kappa^2]\cos(2k_0\eta t)$$
$$-2\exp(-2k_0\kappa t)[4\epsilon\kappa(\epsilon^2-\eta^2-\kappa^2)]\sin(2k_0\eta t)\}\ .$$

The importance of the forbidden band in the study of AFMR linewidths can now be seen. Note that, for large values of κ, the transmission coefficient is proportional to $\exp(-2k_0\kappa t)$. Therefore, the transmis-

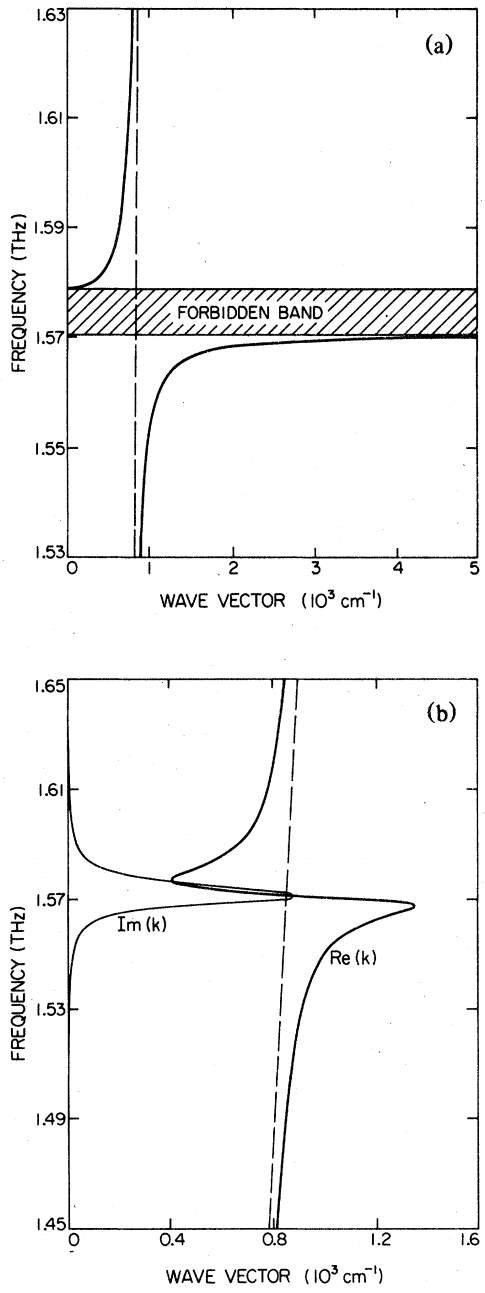

FIG. 4. Theoretical polariton dispersion of pure FeF_2 is shown in (a) for the case of no damping ($\Delta H=0$) and $H_0=0$. (Splitting of the upper and lower AFMR branches would occur for $H_0\neq 0$.) Near zero-field AFMR frequency ν_H^0 there exists a forbidden band within which wave vector k has no real component. Far from ν_H^0, the polariton dispersion converges to that of light (dashed line). In (b), damping is included ($\Delta H=2$ kOe). In the region corresponding to the forbidden band in (a), k now has both real (heavy line) and imaginary (thin line) parts, so polaritons may propagate at all frequencies, though they are strongly attenuated when $\mathrm{Im}(k)$ is large.

sion through a sample as a function of frequency is small for frequencies within the forbidden band, where the wave vector is pure imaginary. This produces a line profile which has an *apparent* width determined not only by intrinsic relaxation processes (yet to be included), but in large part by the forbidden band itself.

An observed transmission spectrum for FeF_2 is shown in Fig. 1. The frequency was held constant while H_0 was varied. By comparison with the dispersion relation (shown on the same figure) the important spectral features $(A-F)$ can be easily understood. Far-off resonance (A,F) k is entirely real and varies slowly with H_0; therefore, the transmission, which depends on thickness and wave vector $[(k \simeq (\omega/c_0)\sqrt{\epsilon}$ in this region], is almost constant. Approaching the resonance position (from either side), $\mathrm{Re}(k)$ varies rapidly and gives rise to the interference peaks which are labeled by B and E. At the resonance position the imaginary component of

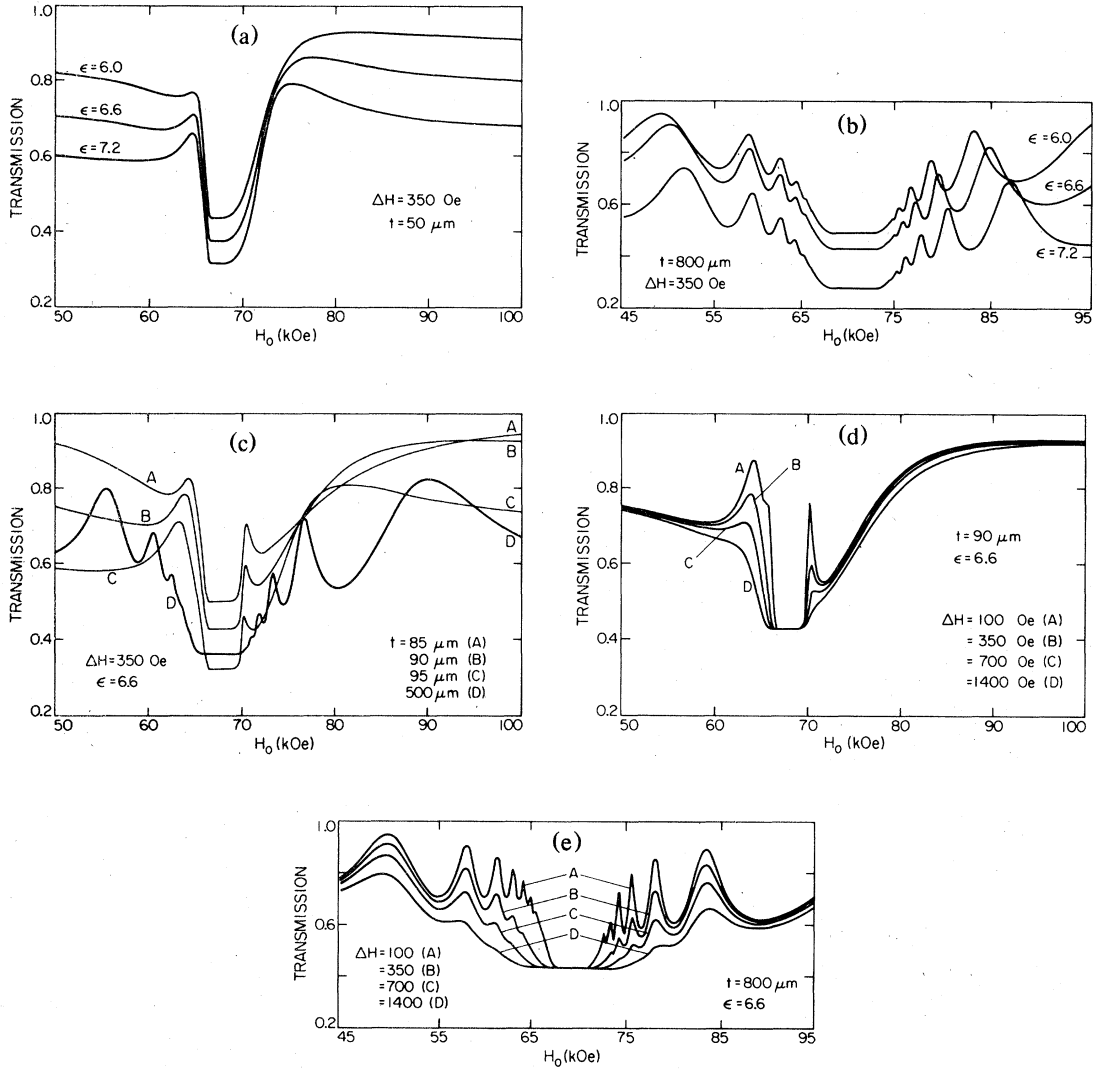

FIG. 5. Effects of thickness t, dielectric constant ϵ, and linewidth ΔH on transmission vs H_0 are illustrated by fixing two of the parameters and varying the third in the polariton model. In (a), variations in ϵ for a *thin* sample are seen to change the relative shape and the amplitude of the off-resonance wings. In (b), variations of ϵ in a *thick* sample are seen not only to change the off-resonance background, but also to shift the positions of the "interference peaks." In (c), t is varied and ϵ is fixed. Since ϵ and t together determine the optical thickness, varying t is seen to have similar effects as varying ϵ. In (d) and (e), ΔH is varied for a thin and thick sample, respectively. As ΔH increases, the AFMR profile is broadened, and small "interference peaks" are smeared, but the effects are most dramatic in the thick sample. Hence the thick samples were used for determination of ΔH, as discussed in the text. See also Fig. 6.

wave vector rapidly varies from zero to its maximum value, causing the sharp slope labeled C. The sharp corner corresponds to the AFMR position for the lower branch where the "−" polarization radiation is completely absorbed. The flat portion of the curve at D is a consequence of the forbidden band. Since the extinction coefficient depends on the exponent (κt), transmission in the forbidden band depends on both wave vector and thickness. Therefore, for a given thickness, there is a finite range of $\mathrm{Im}(k)$ where the "−" polarization radiation is almost completely absorbed.

It is to be noted that no *spatial* dispersion of magnons appears in this treatment. Spatial dispersion [i.e., $\mu=\mu(\vec{k},\omega)$] introduces a second degenerate solution at frequencies above the gap.[10] In the case of *magnetic* polaritons, the second solution lies at such large wave vectors that it is not appreciably excited and may be ignored. In this respect, magnetic polaritons are more amenable to study than other types of polaritons which have degenerate solutions of comparable k. In those systems, a transmission calculation [as in Eq. (8)] usually requires a microscopic model of the sample boundaries in order to partition energy between the two possible modes.[10]

The polariton model may be extended to include damping by letting $\omega \rightarrow \omega + i\Delta\omega$ in Eq. (1), where the damping parameter $\Delta\omega$ is related to the linewidth ΔH (full width at half maximum, in field units) by $\Delta\omega = \frac{1}{2}\gamma(\Delta H)$. This substitution is completely equivalent to adding a Bloch-type relaxation term to the linearized magnetization equations of motion. The effect of damping on polariton dispersion is shown in Fig. 4(b). For frequencies within the band, k is no longer pure imaginary, but has both real and imaginary parts. The singularity in $\mathrm{Re}(k)$ is removed, and as $\Delta\omega$ increases, the extreme values of $\mathrm{Re}(k)$ are depressed toward the dispersion curve for light. $\mathrm{Im}(k)$, which may be interpreted as an attenuation constant, has a peak value at the AFMR frequency. As $\Delta\omega$ increases, $\mathrm{Im}(k)$ is broadened, its peak value diminishes, and the dispersion becomes less asymmetric.

In order to determine the intrinsic linewidth, ΔH, from the data it is necessary to make a detailed comparison with the model. The computer-generated transmission spectra shown in Fig. 5 illustrate the effect of changing ΔH, t, and ϵ. Since ϵ and t together determine the optical thickness of the sample, both have similar effects on the spectrum. As shown in Figs. 5(a)–5(c), changing either ϵ or t affects the relative shape and amplitude of the off-resonance wings as well as the position of interference structures (in thick samples). Knowing t accurately enables ϵ to be determined by fitting the positions of these interference peaks. In Figs. 5(d) and 5(e), ΔH is varied; as ΔH increases, the line profile broadens and the interference structures begin to smear.

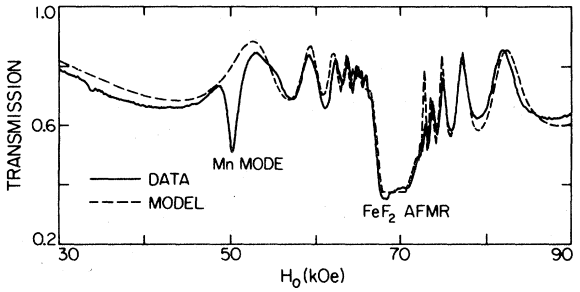

FIG. 6. Transmission data of 1.36-THz radiation vs magnetic field H_0 is compared to the theoretical predictions of the polariton model, for a thick [(786 ± 3) μm] sample of FeF_2:Mn [$c=(0.0014\pm0.0007)$ at.%]. This is a two-equations-of-motion model and hence it neglects the effects associated with the impurity modes. The parameters of the model used are: $\Delta H=20$ Oe, $t=786$ μm, and $\epsilon=5.4$.

The slope near the AFMR position, the width of the flat absorption region, and the intensity of the interference peaks were the chief criteria used in determining the linewidth, ΔH, needed to fit the data.

Experimental results. The solid curve in Fig. 1(a) is the transmission spectrum of a 77-μm disk of FeF_2 obtained at frequency $\nu=1.36$ THz and a temperature of 4.2 K. The resonance at $H_0\simeq50$ kOe, which we will discuss later, results from traces of Mn ions ($\simeq$0.002 at.%). The dashed curve is the model prediction, Eq. (8), from which as we shall see later, an upper bound on the intrinsic linewidth, of $\Delta H\simeq20$ Oe is obtained. Figure 6 shows the spectrum of a thicker disk ($\simeq$786 μm) of FeF_2. Except for thickness, all parameters are identical. Since the relative intensities of the numerous sharp "interference peaks" which appear in the transmission spectrum of the thick sample are very sensitive to the linewidth, a more accurate determination of ΔH is possible than with a thinner sample. The dashed curve is the model prediction which is consistent with the upper bound $\Delta H\simeq20$ Oe obtained for 77-μm sample. We defer further discussion of the line profile and intrinsic width problem until after the effects of the Mn impurity are considered in detail.

IV. Mn IMPURITY MODE

In Sec. III, good agreement between experiment and an AFMR polariton model for FeF_2 was obtained. We now introduce a model which takes the Mn impurity and its associated resonance into account, and which explains several additional features observed in the data, such as impurity-mode enhancement and frequency pulling of both the host AFMR and impurity modes.

We begin from a set of four linearized equations of motion, two for the transverse magnetizations of the

host ($M_{a,b}^{\pm}$) and two for the impurity ($m_{a,b}^{\pm}$).

$$(\omega + i\Delta\omega)M_{a,b}^{-} = -\gamma M_{a,b}^{-}[\pm(\lambda_2' - \lambda_1')m_S \pm H_A \pm \lambda M_S + H_0] \mp \gamma M_S(\lambda M_{b,a}^{-} + \lambda_2' m_{b,a}^{-} + \lambda_1' m_{a,b}^{-} - H_1^{-}) , \tag{9a}$$

$$(\omega + i\Delta\omega')m_{a,b}^{-} = -\gamma' m_{a,b}^{-}[\pm(\lambda_2' - \lambda_1')M_S \pm H_A + H_0] \mp \gamma' m_S(\lambda_2' M_{b,a}^{-} + \lambda_1' M_{a,b}^{-} - H_1^{-}) . \tag{9b}$$

Subscript a (b) indicates the up (down) sublattice.

Equations (9a) and (9b) are written explicitly for the "$-$" sense of polarization, corresponding to the resonance of the lower branch. The "$+$" polarization equations are obtained by reversing the sign of H_0 and of all superscripts. γ', H_A', and $\Delta\omega'$ are, respectively, the gyromagnetic ratio, anisotropy field, and damping parameter of the impurity. The impurity sublattice magnetization, m_s, is the z component of a concentration c of Mn dipoles on a single sublattice. Its value is approximately $640c/100$ Oe in FeF_2 at $T \ll T_N$.

Three types of exchange appear: λ is the exchange constant between oppposite host sublattices. Exchange between host ions on the same sublattice is neglected, because it is very small.[12] However, impurity-host exchange between same (λ_1') and opposite (λ_2') sublattices is included. Positive λ's indicate antiferromagnetic exchange. Because no interaction between impurities is considered, the model is valid only for $c \ll 100\%$, which is the region of experimental interest. The range $0 \leq c \leq 100\%$ may be modeled using the same approach, the result of which is shown in Appendix B.

Since in Eq. (9b) the exchange terms which couple the impurity to the host play the same role as $H_1^{\pm}$, we can write an effective driving field (written explicitly only for m_b^{-}) by

$$H_{\text{eff}} \equiv H_1^{-} - \lambda_1' M_b^{-} - \lambda_2' M_a^{-} = \Lambda H_1^{-} , \tag{10}$$

where Λ is the enhancement factor given by $\Lambda \equiv (1 - \lambda_1' M_b^{-}/H_1^{-} - \lambda_2' M_a^{-}/H_1^{-})$. Note that Λ depends on both the proximity of the impurity resonance to the host AFMR (through the value of M_a^{-} and M_b^{-} at the impurity resonance position) and on the exchange coupling λ_1' and λ_2'. Equations (9a) and (9b) may be solved for the total enhanced transverse susceptibility,

$$\chi_{\text{tot}}^{\pm} = \sum_{i=a,b} \frac{(M_i^{\pm} + m_i^{\pm})}{H_1^{\pm}} , \tag{11}$$

which replaces Eq. (1) in a polariton-transmission calculation.

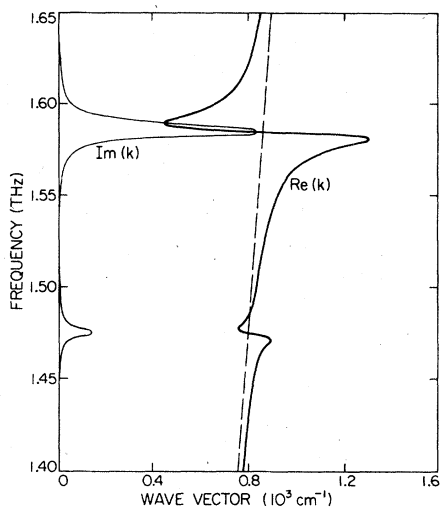

FIG. 7. Polariton dispersion is shown for the four-coupled-equations-of-motion model with $\Delta H_H = \Delta H_1 = 2$ kOe. The resonance-associated structure at the AFMR frequency shown in Fig. 4(b) (no impurity) occurs now at both the AFMR and impurity-mode frequencies. Again, the dashed line is the dispersion of light.

The dispersion calculated from this coupled impurity-host magnetization model is shown in Fig. 7. In Fig. 8 we compare the transmission predicted by this model to that of an "uncoupled" one, obtained by setting $m_{a,b}^{\pm} = 0$ in Eq. (9a) and $M_{a,b}^{\pm} = 0$ in Eq. (9b). With respect to the uncoupled model, we find that the modes are shifted apart (frequency pulling) as a function of c, the impurity mode is more intense (enhancement) and a broad impurity mode can broaden the host mode (linewidth transfer). This latter point will be discussed in Sec. V in more detail.

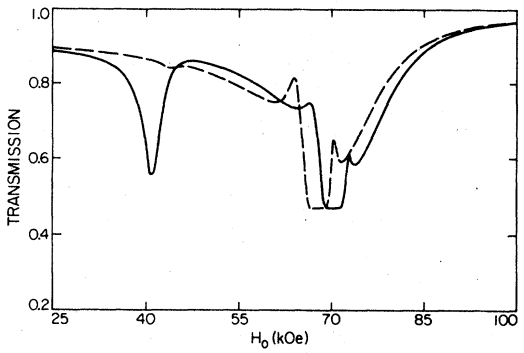

FIG. 8. Theoretical predictions of the four-coupled-equations-of-motion model (solid lines) are compared to the uncoupled model (dashed lines), for lower-branch resonances at $\nu = 1.36$ THz, $c = 0.1$ at.%, $\Delta H_H = 350$ Oe, and $\Delta H_1 = 2.5$ kOe. The transmission is plotted vs H_0 and the effects of frequency pulling and enhancement are clearly visible.

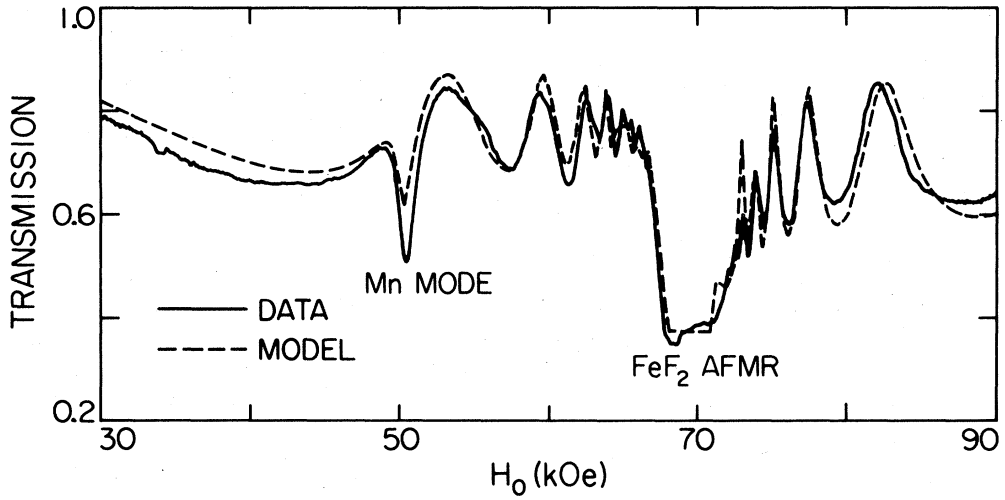

FIG. 9. Transmission vs field data are compared to theoretical predictions of the four-equations-of-motion polariton model for the same thick sample of Mn:FeF_2 shown in Fig. 6. Now the impurity mode appears at its proper position but little else is changed in the calculated spectrum in Fig. 6. The model parameters used are: $\Delta H = 20$ Oe, $t = 786$ μm, $\epsilon = 5.4$, $c = 0.002$ at.%, $\lambda_1' = 300$, and $\lambda_2' - \lambda_1' = 394$.

Experimental results

The solid curve in Fig. 9 is a transmission spectrum of a thick disk of FeF_2:Mn ($t = 786 \pm 3$ μm, $c = 0.0014 \pm 0.0007$ at.%, $\omega = 1.36$ THz, $T = 4.2$ K). The dashed line is the synthetic spectrum generated by computer from the coupled model, $c = 0.002$ at.%, $\Delta H_H = 20$ Oe, $\Delta H_1 = 1$ kOe, $\lambda_1' = 300$, $\lambda_2' = 1234$. Now we see that nearly all spectral features of the data are reproduced by the model, including the impurity-mode position and width.

Figure 2 shows the resonance positions observed in a sample with $c \simeq 0.01$ at.%, $T = 4.2$ K, at several FIR frequencies. Using these data (assuming a linear splitting of the resonances with applied field), the zero-field resonance frequencies of the host and impurity mode are obtained as $\nu_H^0 = 1.575 \pm 0.001$ THz and $\nu_1^0 = 1.507 \pm 0.001$ THz, respectively. The corresponding g values are $g = 2.22 \pm 0.01$ and $g' = 2.05 \pm 0.01$. Values determined for other concentrations appear in Table II.

ν_H^0 and ν_1^0 are plotted versus c in Fig. 10. The curves shown are the frequency-pulling predictions of the coupled model for various choices of λ_1'. The quantity $(\lambda_2' - \lambda_1')$ is required to be equal to 937 ± 5 to fix the position of the mode at $c = 0$, as seen from the Ising expression[13] $\omega_1 = \gamma'[(\lambda_2' - \lambda_1') M_S + H_A' - H_0]$, using $\nu_1^0(c = 0) = 1.51$ THz, $H_A' \simeq 8$ kOe, and $M_S = 560$ Oe. [Note that the Ising expression is reproduced by Eq. (9b) in the limit $c \simeq 0$.] The best fit is obtained for a value of $\lambda_1' = 300 \pm 50$. The positive sign of λ_1' implies the impurity ions are antiferromagnetically coupled to host ions on the same sublattice, in agreement with the NMR results of Riedi *et al.*[14] Defining J_1' and J_2' in the Ising ap-

TABLE II. Zero-field resonance frequencies and g factors (as determined from data similar to that shown in Fig. 2) are tabulated for four concentrations of FeF_2:Mn.

c (at.%)	ν_H^0 (THz)	ν_1^0 (THz)	g	g'
$(1 \pm 1) \times 10^{-2}$	1.575 ± 0.001	1.507 ± 0.001	2.22 ± 0.01	2.05 ± 0.01
$(2.8 \pm 0.3) \times 10^{-1}$	1.587 ± 0.002	1.497 ± 0.002	2.21 ± 0.001	2.07 ± 0.02
$(5.2 \pm 0.5) \times 10^{-1}$	1.590 ± 0.001	1.487 ± 0.004	2.20 ± 0.01	2.09 ± 0.04
$(7.5 \pm 0.7) \times 10^{-1}$	1.601 ± 0.001	1.481 ± 0.006	2.20 ± 0.01	2.07 ± 0.04

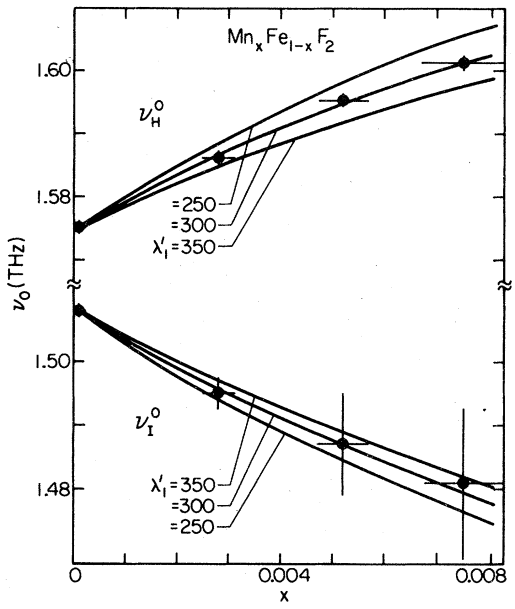

FIG. 10. Measured zero-field resonance positions of both host (ν_H^0) and impurity (ν_I^0) modes are plotted vs concentration and compared to the coupled-model predictions (curves) for various values of intrasublattice, impurity-host exchange parameter λ_1'. Best agreement is obtained for $\lambda_1' \simeq 300$, $\lambda_2' - \lambda_1' \simeq 937$ (positive sign indicates antiferromagnetic exchange).

proximation

$$\omega_1^- = \gamma' H_A' - \gamma' H_0 + (2S/\hbar)(8J_2' - 2J_1') \ ,$$

we obtain $J_1' = 2.0 \pm 0.2$ cm^{-1}, $J_2' = 2.04 \pm 0.05$ cm^{-1} for host-impurity exchange in FeF_2:Mn. In Table III these values are compared with the host-host exchange constants in FeF_2 and MnF_2, and the host-impurity exchange in MnF_2:Fe.

TABLE III. Host-impurity exchange constants in FeF_2:Mn and MnF_2:Fe and host-host exchange constants in MnF_2 and FeF_2 are tabulated. $J > 0 (< 0)$ indicates antiferromagnetic (ferromagnetic) exchange.

	FeF_2:Mn	MnF_2:Fe[a]	MnF_2[b]	FeF_2[c]
J_1 (cm^{-1})	2.0 ± 0.2	-0.70	-0.22	-0.024 ± 0.030
J_2 (cm^{-1})	2.04 ± 0.05	1.42	1.22	1.82 ± 0.05

[a]A. R. Oseroff and P. S. Pershan, in *Light Scattering in Solids*, edited by M. Balkinsi (Flammarion Science, Paris, 1971).
[b]A. Okazaki, K. C. Turberfield, and R. W. Stevenson, Phys. Rev. Lett. 8, 9 (1964).
[c]Reference 12.

V. LINEWIDTHS

The interpretation of the linewidth data for the impurity and host modes is complicated by the interaction between the two. Nevertheless, we have been able to determine that at 4.2 K, the host linewidth is $\Delta H_H = 20 \pm 10$ Oe, for a Mn concentration $c = 0.001$ at.% and that of the impurity linewidth is $\Delta H_1 \simeq 1$ kOe. At this small value of c, the impurity mode, which appears to have a Lorentzian line profile, is clearly much broader than the host mode. While it is true that an excitation localized on an Mn impurity should exhibit ^{55}Mn plus ^{19}F hfs spread over 600 Oe,[15] this cannot account for the observed ΔH_1. For higher Mn concentrations ($c \simeq 0.01$ at.%) both host and impurity modes broaden with increasing c. However, it is always the case that $\Delta H_1(c) >> \Delta H_H(c)$ and $\Delta H_1 = \Delta H_1(c,t)$, whereas ΔH_H depends only on c and not on t, where t is the sample thickness.

A. Radiative contributions to ΔH_1; $T << T_N$

An indication of a possible broadening mechanism comes from the explicit dependence of ΔH_1 on sample thickness t, as shown in Fig. 11. Previous experience[2] on the AFMR of MnF_2 at 23 GHz leads us to

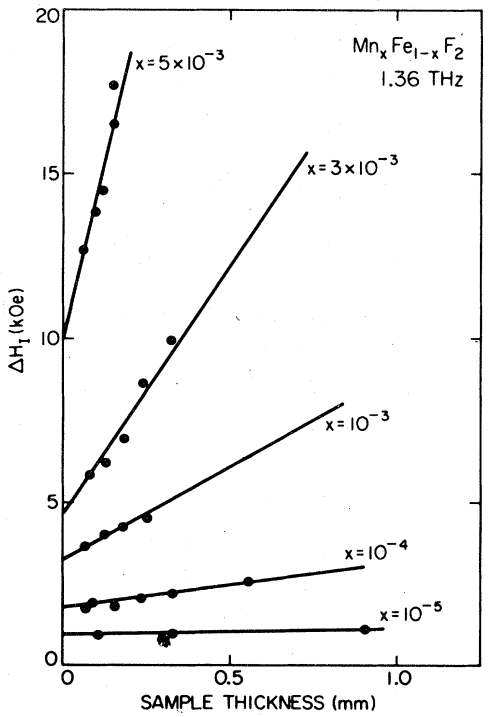

FIG. 11. Observed ΔH_1 vs sample thickness is shown for several concentrations of Mn in FeF_2. The straight lines are best fits to the data; their slopes determine the radiative contribution to ΔH_1.

associate a sample-size-dependent linewidth with a radiation damping mechanism. Equating the power radiated by a precessing magnetic dipole moment with the power absorbed by the spin system in a rf field leads to the following expressions (in the point-dipole approximation[16]) for the "free space" FMR and AFMR linewidths, respectively, arising from radiation damping, FMR:

$$(\Delta H)_0^{\rm rad} = \tfrac{4}{3} M_S V \left(\frac{\omega}{c_0}\right)^3 , \tag{12}$$

AFMR:

$$(\Delta H)_0^{\rm rad} = \tfrac{4}{3} M_S V \frac{H_A}{H_C} \left(\frac{\omega}{c_0}\right)^3 , \tag{13}$$

where V is the sample volume. At microwave frequencies the sample dimension d is small compared to the radiation wavelength λ and Eqs. (12) and (13) are appropriate. However, since the AFMR of FeF_2 occurs in the FIR, where sample dimensions are not negligible compared to the wavelengths, it is necessary to consider propagation through the sample. A convenient approach to the FIR problem (when $d \gtrsim \lambda$) is obtained by adapting a theory of superradiance[17] to a magnetic dipole density. This results in a smaller linewidth than would be obtained in the $d \ll \lambda$ limit since the phases of both the incident and radiated waves vary throughout the sample and destructively interfere. The linewidth is given by $(\Delta H)^{\rm rad} = \mu (\Delta H)_0^{\rm rad}$ where μ depends both on the sample geometry and $\vec{k}$.

In the flat-disk geometry, with $\vec{k} \perp$ to the plane of the disk, $(\Delta H)^{\rm rad}$ depends on thickness t, but not on the lateral dimensions.[17] For the AFMR mode, the radiative width is given by

$$\Delta H_H^{\rm rad} = 2\pi k_0 M_S \frac{H_A}{H_C} t \left[1 + \frac{\sin^2(\sqrt{\epsilon} k_0 t)}{(\sqrt{\epsilon} k_0 t)^2}\right] , \tag{14}$$

where $k_0 = \omega/c_0$. Inserting $t = 88$ μm, a width of 3.5 kOe is obtained (at $\omega/2\pi = 1.36$ THz). Not only is this an order of magnitude larger than the observed ΔH_H (for $c \simeq 0.01$ at.%), but the latter does not vary with t, as Eq. (14) suggests. Both aspects of this dilemma are a consequence of the polariton gap.

The absence of t dependence in ΔH_H may be understood from Eq. (1) with damping included. Since the imaginary part of $k^{\pm}$, $\mathrm{Im}(k^{\pm})$, is the attenuation constant for polaritons within the sample, a transverse magnetization is induced only within an effective thickness $t_{\rm eff} \equiv 1/\mathrm{Im}(k)$. When $t >> t_{\rm eff}$, changing t does not change the effective sample size. The implication of this is that, for an order-of-magnitude estimate of the radiative linewidth, t should be replaced by $t_{\rm eff}$ in Eq. (14), which becomes

$$\Delta H_H^{\rm rad} \simeq 2\pi k_0 M_S \frac{H_A}{H_C} t_{\rm eff} \left[1 + \frac{\sin^2(\sqrt{\epsilon} k_0 t_{\rm eff})}{(\sqrt{\epsilon} k_0 t_{\rm eff})^2}\right] . \tag{15}$$

In the absence of damping ($\Delta H_H \to 0$), $\mathrm{Im}(k)$ approaches infinity at the AFMR position and $t_{\rm eff} \to 0$. It follows that *without nonradiative damping there will be no penetration of radiation into the sample and hence no radiation damping.* When nonradiative damping is introduced, $\mathrm{Im}(k)$ on resonance decreases, thereby increasing $t_{\rm eff}$ and resulting in a larger radiative contribution. For example, when $c = 0.01$ at.%, the observed linewidth $\Delta H_H \simeq 350$ Oe, corresponds to a value of $\mathrm{Im}(k^-) \simeq 2000$ cm^{-1} on resonance and $t_{\rm eff} = 1/\mathrm{Im}(k^-) \simeq 5$ μm $<< t$. For these values, Eq. (15) yields $\Delta H_H^{\rm rad} \simeq 370$ Oe. Since $\Delta H_H^{\rm rad} \gtrsim \Delta H_H$, it is clear that the choice of $t_{\rm eff} \equiv 1/\mathrm{Im}(k)$ somewhat overestimates the radiative contribution.

On the other hand, one *does* expect t dependence in ΔH_1, because the radiation penetrates the entire sample on resonance. [This is confirmed by Fig. 1(a)]. An expression for $(\Delta H)_0^{\rm rad}$ is obtained from Eq. (12) by choosing M_s to be the *enhanced* impurity sublattice magnetization, i.e, $M_S \to \Lambda M_S$, where Λ is calculated using Eq. (10) (or equivalently by taking the ratio of the on-resonance values of the impurity-mode susceptibility obtained from the coupled and uncoupled models). By so doing, the following expression for the radiative linewidth for the impurity is

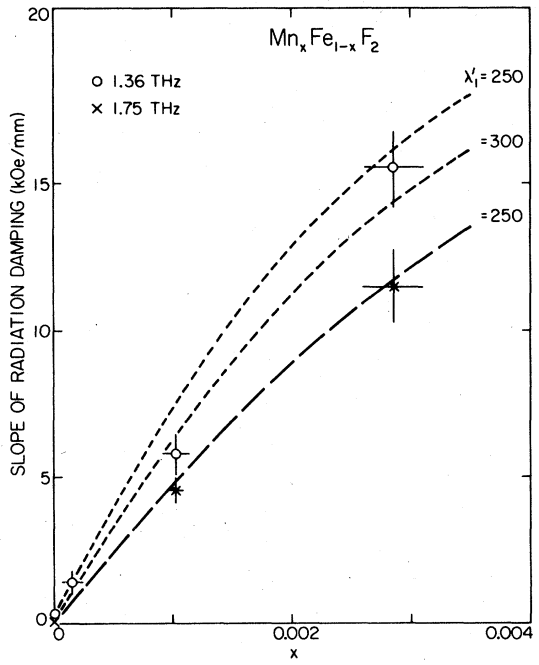

FIG. 12. Slopes, $\Delta H_1^{\rm rad}$ divided by thickness, obtained from Fig. 11, are plotted vs Mn concentration. The curves are the predictions of the four-coupled-equations-of-motion model for various choices of λ_1'. The value of $(\lambda_2' - \lambda_1') \simeq 937$ is set by the zero-concentration impurity-mode position.

obtained,

$$\Delta H_1^{\text{rad}} = 2\pi k_0 \Lambda M_S t \left[1 + \frac{\sin^2(\sqrt{\epsilon} k_0 t)}{(\sqrt{\epsilon} k_0 t)^2}\right] . \quad (16)$$

Note the absence of the factor H_A/H_C in ΔH_1^{rad} as compared with ΔH_H^{rad} for the host AFMR.

The slopes, ΔH_1^{rad} divided by thickness, are obtained from the graph of ΔH_1 versus thickness (Fig. 11) and are plotted versus Mn concentrations in Fig. 12. The curves shown are the predictions of the coupled-equations-of-motion model for various choices of λ_1'. It is comforting to find that the exchange parameters which provide the best fit are consistent with those values which were obtained from frequency-pulling data, namely, $\lambda_1' = 300 \pm 50$, $\lambda_2' - \lambda_1' \simeq 940$.

B. Intrinsic (nonradiative) contributions to ΔH; $T \ll T_N$

Since the radiative, ΔH^{rad}, and nonradiative, ΔH^{int}, contributions to ΔH (host or impurity) are uncorrelated, we may assume the two to be additive ($\Delta H = \Delta H^{\text{rad}} + \Delta H^{\text{int}}$), provided ΔH^{int} is associated with a Lorentzian line profile. In the case of the host linewidth, ΔH_H, some uncertainty exists as to the exact radiative contribution as discussed in Sec. V A. Although this limits the accuracy with which a quantitative determination of ΔH_H^{int} can be made, there are certain qualitative features which can be inferred.

We have calculated[9] the two-magnon imperfection scattering arising from dipolar (pit) or impurity effects, using the Loudon-Pincus[18] formalism. For a thin slab ($t = 100$ μm, $N = 0.5$, pit size $= 1$ μm) we obtain a value of $\Delta H_H(\text{pit}) = 2$ Oe, not unlike that found for MnF_2.[1] For the host-impurity two-magnon exchange (including both $\Delta J_1'$ and $\Delta J_2'$) and anisotropy scattering, we obtain values of 1.3 and 0.5 Oe/%, respectively. None of these explains the observed increase in ΔH_H from 20 Oe at $c = 0.001$ at.% to 350 Oe at $c = 0.01$ at.%, even though most of the observed linewidth may be of radiative origin. In fact, it would not be misleading to state that impurity two-magnon scattering is 2–4 orders of magnitude too small to explain the Mn-impurity c-dependent contribution to the linewidth. We will return to consider the possible origin of the host AFMR linewidth after a discussion of the impurity-mode width.

As to the intrinsic contributions to the impurity-mode widths, it first should be restated that for all concentrations $\Delta H_1 \gg \Delta H_H$. It is also clear from Fig. 11 that a large, c-dependent linewidth ΔH_1^0 persists in the $t = 0$ limit. Since, even for $c \simeq 10^{-3}$ at.%, ΔH_1^0 is 50 times ΔH_H, it is unlikely that strain-induced variations in the exchange and anisotropy parameters could be the cause.

Wiecko and Hone,[19] using a Green's-function technique, have calculated the broadening due to random spatial "diagonal" disorder in an impure ($c < 1$ at.%) bcc Heisenberg antiferromagnet with exchange only between body center and corner ions taken into account. For frequencies near that of the impurity local mode, the dynamics are described by an effective tight-binding Hamiltonian where the dynamical entities are the local modes associated with each impurity site. In the limit of $c = 0$, the local-mode wave functions have virtually no spatial overlap; therefore, the modes associated with each impurity are dynamically independent. As the concentration grows, the impurity wave functions increasingly overlap, leading, as in the usual tight-binding approximation, to an effective interaction between local modes; the spectrum broadens from a sharp line into a band.

ΔH_1^0 for Mn in FeF_2 is plotted versus concentration for the lower (1.36 THz) branch resonance in Fig. 13. The prediction of the Wiecko and Hone model for the disorder broadening of the $q = 0$ response at 0 K using the parameters appropriate to the lower-branch resonance of the Mn local mode in FeF_2, is shown by the dashed curve.

Note that the data in Fig. 13 show a large impurity linewidth $\Delta H_1 \simeq 1$ kOe in the low-concentration limit which is not explained by the Hone-Wiecko theory or any model which depends on impurity-impurity interactions. Nor can this puzzlingly large residual linewidth be accounted for by hyperfine structure (hfs), strain-induced broadening, or random impurity dipolar shifts. Although the width of an isolated Mn^{2+} hfs spectrum is $\simeq$600 Oe [e.g., Mn^{2+} in ZnF_2 (Ref. 15)] it is expected that the hfs in FeF_2 would be substantially narrowed as long as the dynamical interactions are much larger than the hf fields. If the hf fields were comparable to or greater than the impurity-impurity interactions, the resultant spectrum would have a flat-topped lineshape unlike that which

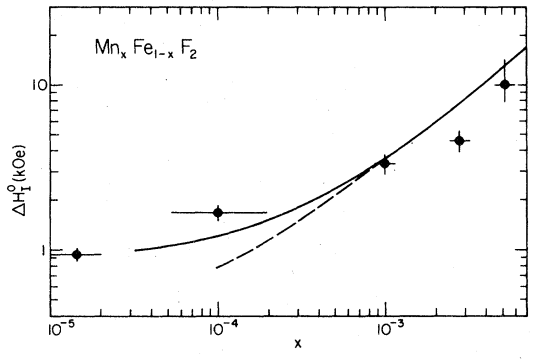

FIG. 13. c-dependent impurity linewidth, ΔH_1^0, as obtained from the $t = 0$ intercept in Fig. 11, is plotted vs concentration for the lower branch resonance (1.36 THZ). The curves, which are discussed in the text, are predictions of the Wiecko-Hone theory.

is observed at low c. A strain-induced mechanism is also an unlikely cause of the residual broadening, since the rms variations in lattice parameters would equally broaden the host AFMR, which depends on both H_A and H_E. Another improbable cause would be dipolar shifts caused by substitution of a nonmagnetic impurity, since a concentration as high as 10% would still not account for the observed linewidth.[9]

Clearly the origin of the large low-concentration impurity-mode linewidth is not understood. Since it is almost certainly uncorrelated with a c-dependent linewidth, it may be appropriate to add $\Delta H \simeq 1$ kOe of broadening to the dynamical broadening in attempting to explain the c dependence of the linewidth, as Hone and Wiecko[19] have done. Their result appears as the solid curve in Fig. 13, which shows qualitative agreement with the data.

ΔH_1^0 for FeF_2:Mn has also been measured on the upper branch (1.75 THz): 3 kOe [$c = (1.4 \pm 0.7) \times 10^{-3}$ at.%], 4.7 kOe [$c = (1.0 \pm 0.1) \times 10^{-2}$ at.%], 6.4 kOe [$c = (3 \pm 0.3) \times 10^{-1}$ at.%], and 7.3 kOe [$c = (5 \pm 0.5) \times 10^{-1}$ at.%]. Linewidth errors are approximately ±10%.

At still higher concentrations, one expects the impurity mode to exhibit a characteristic polariton shape like that of the host mode. Indeed, such a shape is observed in higher concentration samples and in somewhat lower concentration but very thick samples. Nevertheless, any detailed linewidth analysis is made difficult by the appearance of numerous "pair" impurity modes, some of which overlap the "single" impurity mode. (See Fig. 14.) These will be treated in a later paper.

Returning to the problem of the c-dependent contribution to the host linewidth ΔH_H^{int}, it should be noted that (in the four-coupled-equations-of-motion approach) if the observed impurity-mode damping is in the equations for the impurity magnetization, no damping in the host magnetization equations, the observed linewidths for the host are obtained for $c > 0.01\%$. Although these results are obtained from a phenomenological approach they do suggest that

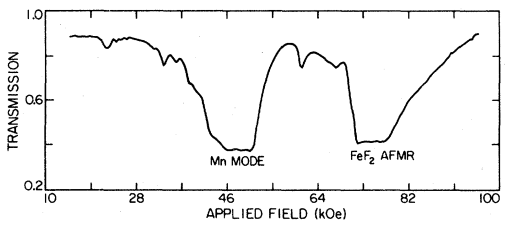

FIG. 14. Observed transmission through FeF_2:Mn vs H_0 for $\nu = 1.36$ THz, $c \simeq 0.3$ at.% in a thick ($t \simeq 460$ μm) sample. The Mn mode has a polaritonlike shape, and many additional Mn pair modes are clearly visible.

"linewidth transfer" is to be expected if the impurity and host mode are in close proximity.

C. Temperature dependence of ΔH

The temperature dependence ($4 < T < 30$ K) of both host and impurity modes was determined in a relatively pure sample ($c = 0.01$ at.%) at 1.36 THz. No linewidth changes occur in either mode below 12 K. However, as T increases further, the host mode broadens and shifts to lower field. Since at 1.36 THz we observe resonance on the lower branch, this shift corresponds to a lowering of the gap energy. For the case where $\hbar\omega$ (magnon energy) $>> k_B T$, which is the experimental region of interest, the four-magnon exchange and anisotropy-induced relaxation theory of Rezende and White[3] is readily modified to account for field-induced changes in magnon population. The measured T-dependent linewidth $\Delta H_H(T)$ (circles) is compared to the four-magnon theory (curve) in Fig. 15. The nonradiative contribution to $\Delta H_H(T)$ (crosses) was obtained by first subtracting the radiative linewidth, ΔH_H^{rad}, calculated from Eq. (15). Note that, although the qualitative agreement between

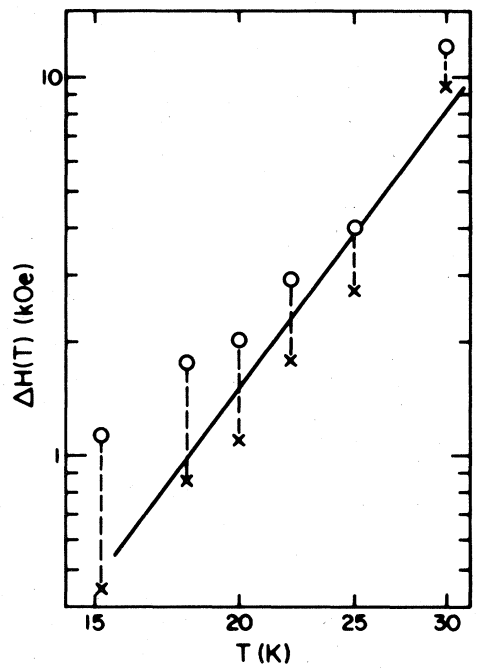

FIG. 15. Comparison between the observed and predicted temperature dependence of the FeF_2 AFMR linewidths. The raw experimental data are shown as open circles; data corrected for radiation damping are shown as crosses. The four-magnon scattering-theory prediction is shown by the solid curve. The measurements were made in a nearly pure sample (Mn impurity concentration, $c \simeq 0.01$ at.%).

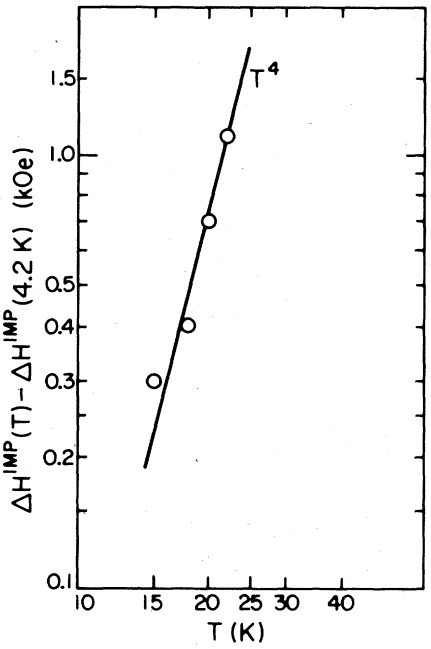

FIG. 16. Mn impurity-mode linewidth ($c \simeq 0.01$ at.%) minus its $T = 4.2$ K value as a function of temperature. The solid line is a best-fit T^4 curve through the data.

theory and experiment is quite good, $[\Delta H_H(T) - \Delta H_H^{rad}(T)]$ is generally lower in field than the theoretical curve. This agrees with our earlier observation that Eq. (15) somewhat overestimates ΔH_H^{rad}, with $t_{eff} \equiv \mathrm{Im}(k)^{-1}$.

The impurity mode shifts with temperature in the same direction as the host mode, but not as rapidly, so that at $T = 25$ K it is overtaken by the host mode and is barely discernible. The *apparent* T-dependent width of the impurity mode increases with temperature approximately at T^4, as is shown in Fig. 16, again indicating four-magnon scattering to be the cause.

VI. SUMMARY

From this combined experimental and theoretical study of the AFMR of FeF_2 and the s_0 local mode associated with a Mn impurity in FeF_2, there has been achieved an understanding of several features pertinent to magnetic-resonance studies in the ordered systems in the FIR. Perhaps most important is that a magnetic-polariton approach correctly describes the observed transmission spectra of the FeF_2 AFMR and implies, thereby, that it will be necessary to do likewise to understand AFMR and related phenomena in the FIR in other materials, such as CoF_2. The upper bound on the intrinsic contribution to the AFMR of "pure" FeF_2 of 20 Oe at 4.2 K demonstrates that uniform-mode excitations in the FIR are not necessarily subject to a large damping effect. That is the case in the microwave region, once super-radiance is properly taken into account.

The study of the Mn impurity mode has shown that the coupled-equations-of-motion model for the impurity and host magnetization works very well in providing a description of the frequency-pulling effects on both host and impurity resonances and correctly yields the magnitude of the enhancement of the latter. The fact that the impurity mode is so much broader than the host for any concentration c may be understood in terms of the Hone-Wiecko theory for impurity-impurity interactions as manifestation of long-range "diagonal" disorder and the larger super-radiant broadening of the impurity resonance resulting from the enhancement and radiation penetration effects.

While we have been able to determine a consistent set of host-impurity exchange parameters using an Ising-like description, it is by no means implied that these are the "true" interaction constants. It is well known[13] that the Green's-function and Ising theories applied to the Mn in FeF_2 problem do not yield the same values for the parameters. This is undoubtedly connected with the fact that the s_0 impurity mode lies too close to the bottom of the host band and causes the impurity wave function to be spatially extended.

Further work is now in progress to understand the pair modes seen at slightly higher impurity concentrations and to compare their positions and intensities with the Green's-function theory.

ACKNOWLEDGMENTS

The research at UCSB was supported by NSF Grant No. DMR77-20185. The authors gratefully acknowledge many helpful discussions with D. Hone and A. R. King. The contributions made by J. P. Kotthaus (laser construction and instrumentation), A. R. King (NMR impurity concentration analysis), and N. Nighman (crystal preparation) have been essential to the success of this work.

APPENDIX A

Consider the transmission of light which is normally incident on a semi-infinite dielectric slab. The geometry and symbols used are shown in Fig. 17 where n, ϵ, μ, and t are the index of refraction, dielectric constant, permeability, and thickness of the slab, respectively.

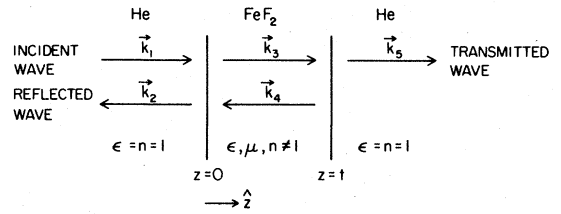

FIG. 17. Geometry of the transmission problem appropriate to a plane wave normally incident upon a dielectric slab as discussed in Appendix A.

The fields are plane waves of the form

$$\vec{H} = \vec{h}\exp(i\vec{k}\cdot\vec{z} - i\omega t) \ ,$$
$$\vec{E} = (n/\epsilon)(\hat{z}\times\vec{H}) \ , \tag{A1}$$

in which $\vec{h}$ and n may be complex. Since n inside the slab is known explicitly for circularly polarized light, and n will be different for the two senses of rotation, it is convenient to treat each polarization separately.

Applying Maxwell's equations leads to the familiar boundary conditions that tangential components of $\vec{E}$ and $\vec{H}$ must be continuous at each interface.[20] At $z=0$

$$h_1 + h_2 = h_3 + h_4 \ ,$$
$$h_1 - h_2 = (n/\epsilon)(h_3 - h_4) \ . \tag{A2a}$$

At $z=t$

$$h_3 e^{ikt} + h_4 e^{-ikt} = h_5 e^{ik_0 t} \ ,$$
$$(n/\epsilon)(h_3 e^{ikt} - h_4 e^{-ikt}) = h_5 e^{ik_0 t} \ . \tag{A2b}$$

From Poynting's vector, $\vec{S} = (c_0/4\pi)(\vec{E}\times\vec{H}^*)$, one obtains the transmission coefficient for polarized light:

$$T = \left|\frac{h_5}{h_1}\right|^2 = \frac{16\epsilon^2 |n\exp(ik_0 nt)|^2}{|(\epsilon+n)^2 - (\epsilon-n)^2\exp(2ik_0 nt)|^2} \ . \tag{A3}$$

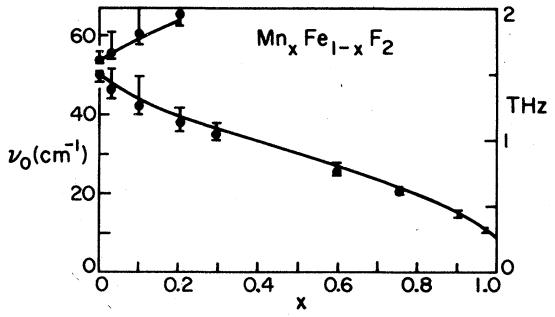

FIG. 18. Resonant frequencies and widths (bars) of FIR absorption lines in $Mn_xFe_{1-x}F_2$ from Enders *et al.* (Ref. 21). The solid curve is the prediction of the four-coupled-equations-of-motion model as discussed in Appendix B.

APPENDIX B

The set of four linearized equations of motion, Eq. (9), can be modified to describe the $Mn_xFe_{1-x}F_2$ system in the concentration range $0 \leq x \leq 1$ by including a MnF_2-MnF_2 exchange, λ'.

$$(\omega + i\Delta\omega)M_{a,b}^- = -\gamma M_{a,b}^-[\pm(\lambda_2' - \lambda_1')m_S \pm H_A \pm \lambda M_S + H_0] \mp \gamma M_S(\lambda M_{b,a}^- + \lambda_2' m_{b,a}^- + \lambda_1' m_{a,b}^- - H_1^-) \ ,$$
$$(\omega + i\Delta\omega)m_{a,b}^- = -\gamma' m_{a,b}^-[\pm(\lambda_2' - \lambda_1')M_S \pm H_A' \pm \lambda' m_S + H_0] \mp \gamma' m_S(\lambda' m_{b,a}^- + \lambda_2' M_{b,a}^- + \lambda_1' M_{a,b}^- - H_1^-) \ . \tag{B1}$$

Four types of exchange now appear: $\lambda(\lambda')$ is the exchange constant between opposite $FeF_2(MnF_2)$ sublattices; $\lambda_1'(\lambda_2')$ is the impurity-host exchange between same (opposite) sublattices. In Fig. 18, data taken from Enders *et al.*[21] are compared to the resonant frequencies calculated from Eq. (B1) as shown by the solid lines. The values of the anisotropy, exchange constants, and magnetization were allowed to vary linearly between the values appropriate for $x=0$ and 1. The agreement appears to be quite good considering the simplicity of the model.

---

*Present address: Laboratory for Atmospheric and Space Physics, University of Colorado, Boulder, Colo. 80309.
†Present address: Faculty of Science, Osaka University, Toyonaka, Osaka, Japan.

[1]J. P. Kotthaus and V. Jaccarino, Phys. Rev. Lett. 28, 1649 (1972); in *Magnetism and Magnetic Materials—1972 (Denver)*, edited by C. D. Graham and J. J. Rhyne, AIP Conf. Proc. No. 10 (AIP, New York, 1973), p. 57.
[2]R. W. Sanders, D. Paquette, V. Jaccarino, and S. M. Rezende, Phys. Rev. B 10, 132 (1974).
[3]S. M. Rezende and R. M. White, Phys. Rev. B 14, 2939 (1976).
[4]J. Barak, S. M. Rezende, A. R. King, and V. Jaccarino, Phys. Rev. B 21, 3015 (1980).
[5]R. C. Ohlmann and M. Tinkham, Phys. Rev. 123, 425 (1961).

[6]P. L. Richards, in *Magnetism and Magnetic Materials—1972 (Denver),* edited by C. D. Graham and J. J. Rhyne, AIP Conf. Proc. No. 10 (AIP, New York, 1972), p. 174.
[7]A preliminary report on this work was given in R. W. Sanders, V. Jaccarino, and S. M. Rezende, Solid State Commun. 28, 907 (1978).
[8]M. Butler, V. Jaccarino, N. Kaplan, and H. J. Guggenheim, Phys. Rev. B 1, 3058 (1970).
[9]R. W. Sanders, Ph.D. thesis (University of California, Santa Barbara, 1978) (unpublished).
[10]D. L. Mills and E. Burstein, Rep. Prog. Phys. 37, 817 (1974).
[11]F. Keffer and C. Kittel, Phys. Rev. 85, 329 (1952).
[12]H. J. Guggenheim, M. T. Hutchings, and B. D. Rainford, J. Appl. Phys. 39, 1120 (1968).
[13]R. A. Cowley and W. J. L. Buyers, Rev. Mod. Phys. 44, 406 (1972).
[14]P. C. Riedi, A. R. King, and V. Jaccarino, Solid State Commun. 29, 701 (1979).
[15]A. M. Clogston, J. P. Gordon, V. Jaccarino, M. Peter, and C. R. Waller, Phys. Rev. 117, 1222 (1960).
[16]S. M. Rezende, in *Meson-Nuclear Data—1972 (Carnegie-Mellon Conference),* edited by P. D. Barnes, R. A. Eisensten, and L. S. Kisslinger, AIP Conf. Proc. No. 34 (AIP, New York, 1976), p. 1. The treatment of radiation damping in FeF_2 in this paper is incomplete, because polariton effects are neglected.
[17]N. E. Rehler and J. H. Eberly, Phys. Rev. A 3, 1735 (1971).
[18]R. Loudon and P. Pincus, Phys. Rev. 132, 673 (1963).
[19]D. Hone and C. Wiecko, J. Magn. Magn. Mater. 15–18, 723 (1980); C. Wiecko and D. Hone, J. Phys. C 13, 3883 (1980).
[20]J. D. Jackson, *Classical Electrodynamics* (Wiley, New York, 1963).
[21]B. Enders, P. L. Richards, W. E. Tennant, and E. Catalano, see Ref. 6, p. 179.